Influence of EGR on Post-Injection Effectiveness in a Heavy-Duty Diesel Engine Fuelled with n-Heptane

Sushant S. Pandurangi, Nicolò Frapolli, Michele Bolla, and Konstantinos Boulouchos
Swiss Federal Institute of Tech.

Yuri M. Wright
ETH Zurich/Combustion+FlowSolutions GmbH

ABSTRACT

Numerical simulations of a heavy-duty diesel engine fuelled with n-heptane have been performed with the conditional moment closure (CMC) combustion model and an embedded two-equation soot model. The influence of exhaust gas recirculation on the interaction between post- and main- injection has been investigated. Four different levels of EGR corresponding to intake ambient oxygen volume fractions of 12.6, 15, 18 and 21% have been considered for a constant intake pressure and temperature and unchanged injection configuration. Simulation results have been compared to the experimental data by means of pressure and apparent heat-release rate (AHRR) traces and in-cylinder high-speed imaging of natural soot luminosity and planar laser-induced incandescence (PLII). The simulation was found to reproduce the effect of EGR on AHRR evolutions very well, for both single- and post-injection cases. Further a direct comparison of the computed and measured temporal evolution of soot luminosity is presented for the 18% initial oxygen volume fraction case. The spatial extents of the predicted spray plumes and soot clouds are in qualitative agreement with experimental data. Subsequently, the model has been used to investigate the effect of the post-injection on in-cylinder soot evolution, especially with respect to the role of increased mixing and temperature; a detailed analysis highlighting the relative importance of soot formation and oxidation (both O_2 and OH contributions) is presented at two representative EGR levels.

CITATION: Pandurangi, S., Frapolli, N., Bolla, M., Boulouchos, K. et al., "Influence of EGR on Post-Injection Effectiveness in a Heavy-Duty Diesel Engine Fuelled with n-Heptane," *SAE Int. J. Engines* 7(4):2014, doi:10.4271/2014-01-2633.

INTRODUCTION

The diesel engine has enjoyed immense popularity in the fields of transportation and power generation for decades. While often lauded as the most efficient type of internal combustion engine on account of its high fuel economy and low CO_2 footprint compared to other engines, the diesel engine struggles to keep up with the rapid pace of pollution reduction efforts and legislation. Soot emissions from diesel engines are known to adversely affect the environment and human health. Due to their mode of operation, involving stratification and presence of fuel-rich, soot-prone regions and simultaneously lean NOx-prone regions in the flame vicinity, a number of challenges are posed, necessitating further research effort into in-cylinder pollutant reduction technologies.

One such approach is exhaust gas recirculation (EGR) which has been studied extensively, especially at low-temperature combustion (LTC) regimes with a focus on NOx reduction (see e.g. [1]). EGR affects combustion by increasing ignition delay, reducing the peak temperature and reducing reaction rates. By itself however, a high level of EGR can cause an increase in the engine-out soot emissions when used in conventional

diesel engines [2, 3] due to the suppression of soot oxidation. This unwanted increase can be countered by adding a small fuel injection, which follows the main injection and is introduced early enough to undergo combustion. The understanding of the efficacy and mechanisms of such post-injections for soot reduction is reviewed in [4] and a detailed experimental study under different EGR conditions (using n-heptane as fuel) is reported in [5].

The computational modelling of diesel engine combustion processes in general poses a number of challenges: highly turbulent and swirling in-cylinder flow coupled with liquid fuel atomization, droplet secondary breakup and evaporation, fuel-air mixing and auto-ignition of complex hydrocarbon fuels followed by premixed and diffusion combustion fuel conversion modes. The modelling of multiple injections involves additional challenges for the correct and separate treatment of each injection. The phenomena related to pollutant generation usually lie at the end of the chain of the above events; the reliable prediction of flow and combustion phenomena is therefore of primary importance for the goal of studying potential reduction of engine emissions.

In combination with computational fluid dynamics, a range of combustion modelling approaches have been applied in recent years ranging from the characteristic time scale (CTC) approach [6], extensions to coherent flame models (ECFM) [7], 2D flamelet models [8], transported probability density function (PDF) methods [9] and presumed PDF methods [10]. The CTC and ECFM models do not require additional modelling for multiple injections and simulation is relatively straightforward. The ECFM-3Z model has been applied [11] to diesel engines for studying the effect of post-injections, and recently the CTC approach [6] has been applied to the same experimental dataset as used in the present study. However, for more elaborate models such as Representative Interactive Flamelets (RIF) or Conditional Moment Closure (CMC) which are based on the mixture fraction, the complexity of the model is considerably increased since two different mixture fractions are needed for describing the two distinct fuel streams. While the first fuel stream exhibits a classical auto-ignition process, the following fuel stream(s) are additionally subject to strong interaction with the preceding stream, which may lead to forced ignition merely due to contact with an established flame [8].

To address these issues, 2D flamelet (RIF) models have been derived [8] and successfully applied to diesel engines [8, 12, 13]. However, difficulties persist in the modelling of terms such as the cross scalar dissipation rate and in obtaining a representative description for the 2D probability distribution needed for convolution. To help reduce such uncertainties, DNS simulations for a three-feed system have been reported in [14] and the processed data supplied as input to separate 2D flamelet calculations. Still, discrepancies were found with respect to heat release rate as well as the evolutions of temperatures conditioned on the respective mixture fractions of the two fuel streams; these were attributed to the use of only one single 2D-flamelet to represent the entire domain. Conceptually, when attempting to incorporate multiple injections into CMC models, difficulties similar to those in the derivation of 2D-RIF can be expected. Additionally, the situation is aggravated by the physical space transport terms in the CMC equations (conditional velocity and conditional turbulent fluxes) [15], for which new closures are likely to be required in the presence of multiple fuel streams. Apart from the modelling challenges, a formal double-conditioning in CMC will also lead to a dramatic increase in computational expense rendering the simulation of diesel engines impractical, since CMC typically discretises the physical domain into thousands of nodes (in contrast to a single 2D flamelet representing the entire domain in the 2D-RIF approach).

The CMC model employed in this study has been successfully and extensively applied to a number of generic test rigs [16,17,18,19,20] and diesel engines [21, 22] using single injections. Extensions to the model have enabled detailed investigations of soot [23,24,25,26] and also the influence of EGR [27] thereupon. Recently the incorporation of arbitrarily spaced multiple injections without requiring formal double-conditioning was reported [28] and successfully applied [29, 30] and the same is used in this work.

The paper is structured as follows. We first discuss the flow field and combustion computation describing the governing equations and the models used. The experimental reference data is then reviewed briefly, followed by results, including validation based on apparent heat-release rates and in-cylinder soot distribution. The results are used to gain an understanding of the effect of EGR on post-injection effectiveness, which forms the subject of discussion, and the main conclusions are then drawn in closing.

NUMERICAL SETUP

The numerical methodology employed in this study follows previous works [23,24,25] except for the model extension to multiple injections. Hence, the latter is described in more detail whereas the rest is only briefly repeated.

Flow Field Computation

The computational domain of the engine is represented as a 45° sector of the entire cylinder, and correspondingly only one of the eight injector holes is considered. The domain is meshed into hexahedral cells with a resolution of 1 mm^3 in the piston bowl resulting in approximately 50,000 cells at top-dead-centre position; at bottom-dead-centre the mesh grows to approximately 240,000 cells. The polar configuration of the CFD mesh is the same as used in [25] wherein a grid sensitivity analysis under non-reactive conditions was also shown. The depth of the piston crevice has been reduced to align it with the piston bowl bottom for simplicity, and consequently its thickness is increased to maintain the overall geometric compression ratio. Figure 1 shows the computational domain along with the individual cells. A coarser-resolution but synchronised mesh of the same model is used for the evaluation of quantities related to the CMC combustion model, which is described in the next section.
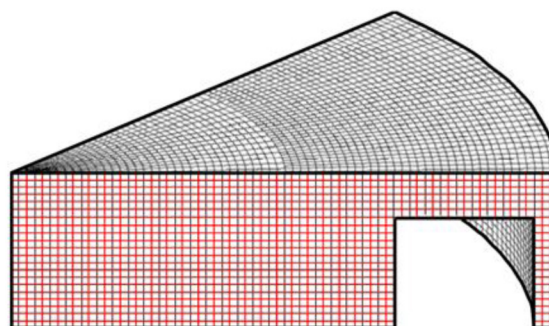

Figure 1. CMC mesh (in red) and CFD mesh (in black) shown overlaid on the same computational domain.

The commercial CFD code STAR-CD [31] has been used to compute the turbulent flow field in the domain. The Reynolds-averaged Navier-Stokes equations are solved with the high Reynolds number *k-ε* model for turbulence. To incorporate the liquid-phase fuel spray in the computation, a Lagrangian approach is used with the 'blob' model for atomization and the model of Reitz & Diwakar [32] for droplet secondary breakup.

The droplets are subject to turbulent dispersion based on a stochastic model. Thermo-physical properties for n-heptane are calculated based on the droplet temperature.

CMC Combustion Model for Single Injection

The conditional moment closure (CMC) model solves transport equations for the conditional mean of temperature and all chemical species, which are weighted with a (presumed shape) beta-PDF function to yield the physical temperature and species fields. The conditioning is performed upon the mixture fraction ξ, for which η denotes the sample space variable, which is resolved with 101 points between the oxidiser and fuel sides ($\xi=0$ and $\xi=1$ respectively) and clustered around the stoichiometric mixture fraction. The conditional expectations of the α-th species mass fraction, Q_α, and temperature, Q_T, are obtained from the following transport equations:

$$\frac{\partial Q_\alpha}{\partial t} + \langle u_j|\eta\rangle \frac{\partial Q_\alpha}{\partial x_j} =$$
$$\langle N|\eta\rangle \frac{\partial^2 Q_\alpha}{\partial \eta^2} + \frac{1}{\rho_\eta \tilde{P}(\eta)} \frac{\partial}{\partial x_j}\left[\langle u_j'' Y_\alpha''|\eta\rangle \rho_\eta \tilde{P}(\eta)\right] + \langle \dot{\omega}_\alpha|\eta\rangle$$

(1)

$$\frac{\partial Q_T}{\partial t} + \langle u_j|\eta\rangle \frac{\partial Q_T}{\partial x_j} = \langle N|\eta\rangle \frac{\partial^2 Q_T}{\partial \eta^2} + \langle N|\eta\rangle \left[\frac{1}{\langle c_P|\eta\rangle}\left(\frac{\partial \langle c_P|\eta\rangle}{\partial \eta} + \right.\right.$$
$$\left.\left. \sum_{\alpha=1}^{N} c_{P,\alpha}\frac{\partial Q_\alpha}{\partial \eta}\right)\right]\frac{\partial Q_T}{\partial \eta} + \frac{\langle \dot{\omega}_H|\eta\rangle}{\rho_\eta \langle c_P|\eta\rangle} + \frac{1}{\langle c_P|\eta\rangle}\left\langle\frac{1}{\rho}\frac{\partial P}{\partial t}\Big|\eta\right\rangle -$$
$$\frac{1}{\rho_\eta \tilde{P}(\eta)} \frac{\partial}{\partial x_j}\left[\langle u_j'' T''|\eta\rangle \rho_\eta \tilde{P}(\eta)\right]$$

(2)

Detailed derivations of the equations are found in [33, 34]. The broad methodology of implementation and CFD-CMC coupling is discussed at length in [21] and is repeated only briefly here. The above equations still contain unclosed terms and a number of sub-models are required for closure. The conditional scalar dissipation rate is treated by the AMC model [35] while a linear relationship is used for the conditional velocity terms. Turbulent fluxes are closed with a gradient flux assumption. The governing equations are discretised with a second-order central differencing scheme for the diffusion terms and an upwind scheme for convective terms. A full operator splitting between the transport in physical and mixture fraction space and chemistry is employed, following conclusions reached in [17]. A stiff integrator is used allowing for substantial performance gains [17].

A simplified reaction mechanism for n-heptane consisting of 22 chemical species in 18 reaction steps is applied [36] based on much success with this compact description in studies of constant-volume combustion [18, 19, 23] as well as diesel engines [24, 25]. Conditional chemical sources are closed at first order; this approach has shown very good results in diesel spray simulations for engines [21, 22] and constant-volume chambers [16,17,18,19,20]. The computational mesh for solving the conditional transport equations is kept coarser than the flow-field mesh; this is made possible due to the much

weaker spatial dependence of conditional quantities compared to their unconditioned counterparts, as shown in [18, 21]. Data mapping between the two meshes is performed at each time step using PDF-weighted averages. Further, as described in detail in [21], the mesh for CMC computations is two-dimensional where the cells have been collapsed azimuthally into a single vertical plane. This provides for a computationally efficient solution in view of the long process duration and computer-intensive chemical reaction integration, where parallelization alone does not offer a satisfactory reduction in computational time.

CMC Combustion Model with Multiple Injections

An extended CMC model is employed in this study, which is able to account for multiple injections using a single total mixture fraction (MFT) as the conditioning scalar [28]. This approach is supported by findings from [8, 12, 13] reporting a rapid transition in 2D flamelet space along the overall stoichiometric mixture, leading to a quasi-1D structure in the MFT coordinate. The reader is referred to [28] for a detailed discussion of the model; only main points are repeated here.

The original temperature and composition, conditional upon the mixture fraction of the first injection (MF1), are transformed into representative profiles that are conditional upon MFT. The spatial resolution of CMC allows for a detailed determination of the time and location of contact between fuel streams, as well as their local conditions. The model is based on re-initialization of the conditional temperature and composition in every CMC cell, at the time of the first appearance of mixture fraction from the second fuel stream (MF2), using localised spatial information. At the time of first MF2 appearance, it is proposed to start from the doubly conditional temperature distribution, as well as the probability distribution of MF1, in the same way as an initialization of doubly conditioned CMC or 2D-RIF [8] as illustrated in Figure 2. MF1 consists of the original burning temperature profile (MF2=0) and adiabatic mixing is assumed along the MF2 coordinate (MF1=const.). Note that the domain consists of a unity triangle, implying that MFT cannot exceed a value of one.
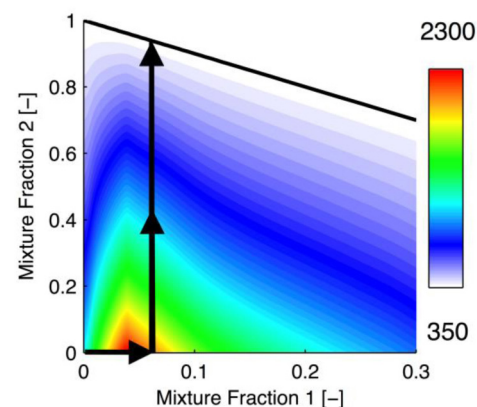

Figure 2. Example of a doubly conditioned temperature distribution at the time of re-initialization.

In order to reconstruct a representative temperature conditioned upon MFT, two fundamental assumptions are introduced: (i) at the time of first appearance of MF2 into a CMC cell, MF1 and its variance both tend to decrease due to convection-diffusion effects and due to the further absence of an MF1 source, implying a temporal separation of MF1 and MF2 sources at a given position; and (ii) when the second fuel stream enters a CMC cell, the increase in MFT is attributed to MF2 only. For the reconstruction of the re-initialised conditional temperature at a given MF1, the left domain of the local MF1 is retained and a vertical line along MF2 is drawn corresponding to adiabatic mixing of the local MF1 with the new incoming MF2, assumed to be the sole MFT source. The new temperature profile, $\langle T_{Double}|\eta_1, \eta_{Tot}\rangle$ for a pre-existing η_1 can be described by:

$$
\begin{aligned}
\langle T_{Double}&|\eta_1, \eta_{Tot}\rangle \\
&= \langle T_{\eta_1}|\eta_{Tot}\rangle[H(\eta_{Tot}) - H(\eta_{Tot} - \eta_1)] \\
&+ \langle T_{mix}|\eta_{Tot}\rangle H(\eta_{Tot} - \eta_1)
\end{aligned}
$$

(3)

Where η_{tot} is MFT, η_1 is the local MF1, H is the Heaviside step function, $\langle T_{\eta_1}|\eta_{Tot}\rangle$ is the original temperature profile before re-initialisation and $\langle T_{mix}|\eta_{Tot}\rangle$ is the mixing temperature obtained following the η_2 coordinate for a constant η_1 on the doubly-conditioned temperature distribution. The probability of encountering a given MF1 inside a CMC cell is assumed to be the current MF1 PDF. The new temperature profile conditional upon MFT, $\langle T_{New}|\eta_{Tot}\rangle$, is computed by considering the marginal PDF for MF1, $P_{\xi_1|\xi}(\eta_1|\eta)$, as $P_\xi(\eta_1)$ owing to the instantaneous initialisation and the subsequent absence of MF2. It follows that:

$$
\langle T_{New}|\eta_{Tot}\rangle = \int_0^1 \langle T_{Double}|\eta_1, \eta_{Tot}\rangle P_\xi(\eta_1)d\eta_1
$$

(4)

The result of the re-initialization described by equations (3) and (4) is illustrated graphically in Figure 3.

The thick black line is the original profile before re-initialization and the array of thin black curves represents the re-initialised temperatures for different MF1 values. The influence of MF1 PDF is illustrated for three different cases: a low mean MF value with low and high variance (MFV) (blue and green respectively) and a high mean MF value with low MFV (red). For cases with low MFV (blue and red), the new temperature is practically a single "cut" at the local mean MF, and for a larger MFV the profile becomes more rounded. Note that the profiles are continuous and differentiable.

The final solution at the CFD resolution relies on conditional expectations of quantities as is typical in the CMC framework, obtained by the convolution (with the MFT PDF) of the new

profile resulting after re-initialization or its time evolution. The effect of localised initialisation is then transported in physical as well as conserved scalar space, as is also the case for single injections. Note that the number of subsequent injections is not limited: it is sufficient to simply re-initialise the profiles whenever fuel from a new injection enters a CMC cell.
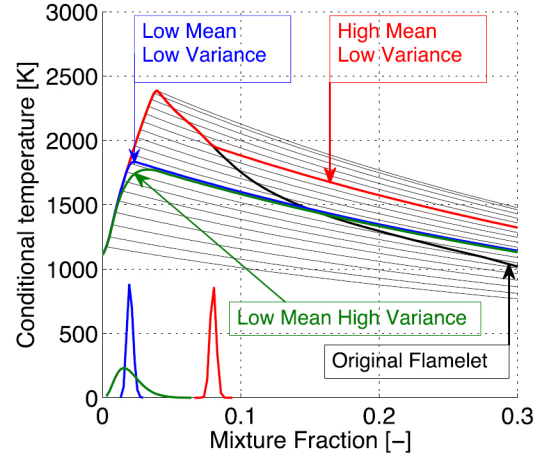

Figure 3. Re-initialised temperature profiles for three different distributions of main mixture fraction.

Soot Modelling

The semi-empirical two-equation model by Leung et al. [37] is used for soot modelling based on prior success in simulations for constant volume test rigs [23] and engines [25]. Transport equations are solved for the conditional mean of soot mass fraction and number. The model considers simultaneous soot inception, surface growth, oxidation by O_2 and OH, and coagulation. Particles are assumed to be spherical and mono-dispersed and a unity Lewis number approach has been considered, neglecting differential diffusion. Acetylene (C_2H_2) is considered as the only soot precursor in this model. The first soot particle consists of 100 carbon atoms [37], corresponding to a primary particle size of 1.28 nm. Chemical reaction rates and constants are described in [24, 25].

EXPERIMENTAL SETUP

High-fidelity experimental data [5] from the optically accessible heavy-duty diesel engine forms the basis of the validation of this study. The engine setup is installed at the Sandia National Laboratories, consisting of the single-cylinder, common-rail direct injection, four-stroke optically accessible engine with eight equally spaced injectors. Windows in the piston and cylinder head enable the imaging of soot by natural luminosity and planar laser-induced incandescence (PLII); details of the setup can be found in [5]. Engine and injector specifications are summarised in Table 1.

From the experimental dataset reported in [5], eight cases have been considered for this study: four levels of EGR resulting in initial ambient oxygen concentrations of 21, 18, 15

and 12.6%, each with and without a post-injection. The main injection is the same as the single injection; the post-injection therefore adds more fuel mass to the combustion. It is worth repeating here from [5] that the engine-out soot, measured by means of the filter smoke number (FSN), initially decreases as the post-injection duration is increased, until a 'minimum soot' condition is reached. After the soot minimum, the slope of the engine-out soot rise with increasing load is steeper than for the baseline single injection. It is the 'minimum soot' condition post-injection that has been considered for the simulations reported here, with a commanded injection duration of 500 μs. The injected fuel mass for the simulations is approximately 74.0 mg for the main and 16.8 mg for the post-injection. The cases are summarised in Table 2:

Table 1. Engine Specifications.

Engine type base	Cummins N-14, Diesel
Displaced volume	2.34 L
Bore and stroke, mm	139.7 mm, 152.4 mm
Bowl width and depth, mm	97.8mm, 15.5 mm
Compression ratio	11.2:1 (geometric)
Fuel injector type	Common rail
Fuel	n-Heptane
Nozzle holes and diameter	8 holes of 0.131mm each
Spray included angle	152°

Table 2. Operating conditions considered for simulation.

Engine speed	1200 RPM
TDC temperature, motored	900 K
Ambient oxygen volume fraction	12.6%, 15%, 18%, 21%
Injection configuration	Main only, Main + post
Injection durations	Main 1950 μs, post 500 μs
Commanded start of injection (main)	347°
Commanded start of injection (post)	366°

A recent numerical study based on the same experimental dataset has been reported in [6] for an EGR level corresponding to 18% ambient oxygen, for several post-injection durations. In this study, we attempt to focus on the effects of varying EGR instead, where detailed chemistry is expected to be more important. To the best of the authors' knowledge, this represents the first study using an elaborate combustion model coupled with soot in the CMC context, for the experimental dataset of [5]. Only one post-injection duration is considered in addition to the single-injection cases for each EGR level.

RESULTS AND DISCUSSION

This section provides a validation of the simulation results by comparison with the experimental AHRR and in-cylinder soot imaging. Simulation results are then analysed in further detail

to try to understand the effect of EGR on interaction between post/main injections and on the in-cylinder soot evolution including formation and oxidation rates.

AHRR Comparisons

AHRR for single- and post-injection configurations over four different EGR levels are shown in Figure 4. Black lines in each case are for experimental data whereas coloured lines represent the simulation results of the respective EGR level. Solid lines are for the post-injection configuration, dashed lines for the single-injection configuration. The injection rate profiles are drawn in dashed lines below the AHRR profiles.

It is to be noted that agreement between simulation and experiment for the single injection cases is of highest importance because the predicted conditions at the end of the main injection are automatically the initial conditions for the post-injection combustion.

For the main injection cases, an excellent agreement for the 21% O_2 is observed for the AHRR evolution, with both the premixed as well as diffusion combustion modes being captured very well. Model predictions become gradually worse by increasing the oxidiser dilution, though still maintaining a good accuracy considering the large dilution spread considered here. In the measurement, as expected, the peak of the premixed combustion mode decreases monotonically with dilution due to the lowered mixture reactivity. The simulation reproduces the correct trend except for the lowest oxygen (12.6%) where the premixed peak becomes higher. This is attributed to the slight over-prediction of the ignition delay in this case due to limitations of the chemical mechanism at less reactive conditions (as reported in [19, 23, 24]), leading to higher heat release in the premixed mode.

For the post-injection cases, from the experimental AHRR it is observed that the EGR level has a minimal influence on the ignition delay of the second injection except for the 12.6% O_2 case. The increase of AHRR induced by the post-injection is also comparable along different ambient dilutions. Concerning the simulation, it is first important to note that the effect of the post-injection on the AHRR is the difference between AHRR with and without post-injection. At the time of start of post-injection, the simulation overestimates the AHRR for the case with main injection only. This offset is reflected in the AHRR with post-injection. For all cases apart from the 12.6% O_2, the time when the AHRR curves with and without post become separated is consistent with the experimental observation. The same applies for the AHRR magnitude as well as the timing of the peak. On the contrary, for the 12.6% O_2 case the simulation shows a faster ignition and conversion of the post fuel. A possible explanation for this is put forth in the discussion section *"Effect of EGR on post-injection effectiveness"* and concerns the possibly premature contact of the tail of the main-flame with the oncoming post-jet.
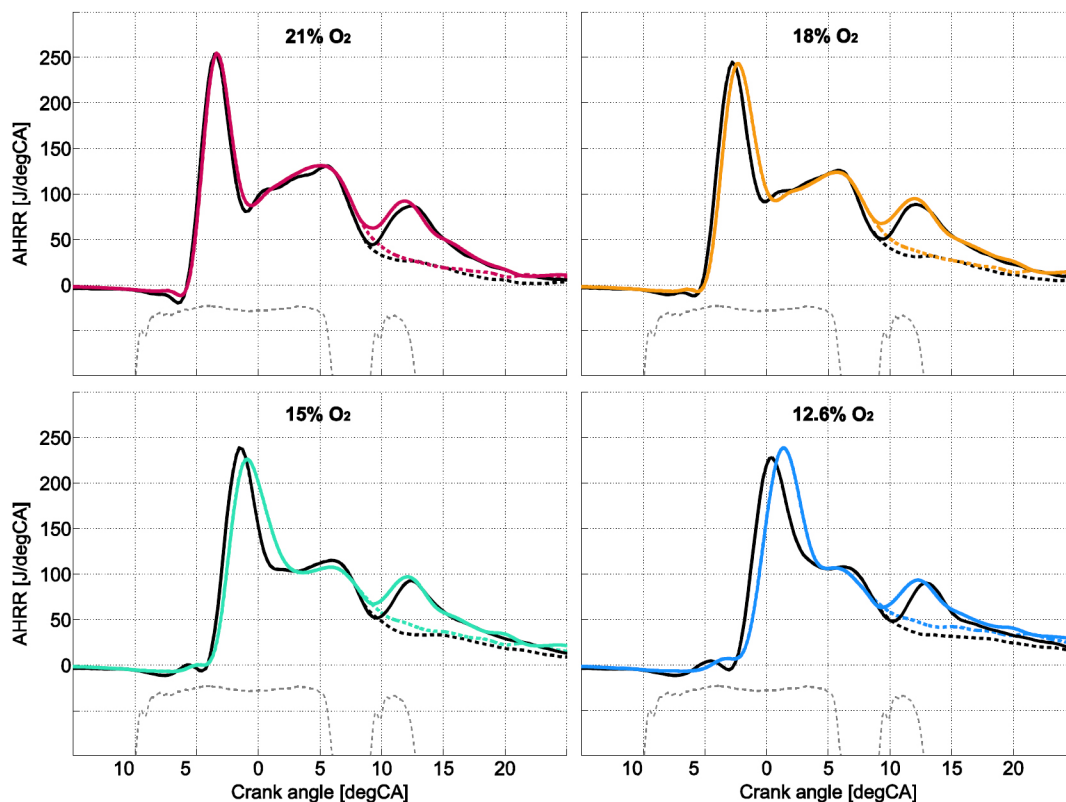
Figure 4. AHRR traces for the considered simulation cases. Black lines: experimental AHRR curves; coloured lines: simulation AHRR curves for the respective EGR level. Dotted lines represent single-injection cases while solid lines represent cases with post-injection. Injection rate profiles are drawn in dashed lines below the AHRR profiles.

Luminosity/PLII and CFD Comparison

The ignition of the post-injection is much more sensitive to the existing flow and thermal fields than the main injection [29]. We denote the 18% O_2 case as the "reference case" and the validation of this case with optically available data will be discussed next.

The three-dimensional soot fields predicted by the simulation can be validated qualitatively against the experimentally obtained Soot-NL and Soot-PLII images. The processing of the 3D CFD data is done as follows: for comparison with the PLII images, the computed soot volume fraction is plotted on a plane along the nominal spray axis, in accordance with the laser-sheet orientation shown in [5]; it is referred to as 'CFD Planar FvS'. For the comparison with experimental Soot-NL, the soot volume fraction is integrated in the cylinder-axial direction and plotted on a cylinder cross-sectional plane, and is referred to as 'CFD Integrated FvS'. A more elaborate post-processing methodology accounting for soot radiation absorption as proposed in [25] has not been attempted, since the soot region is of interest here rather than a quantitative comparison. Representative envelopes are drawn around the soot clouds to improve their demarcation from regions devoid of soot. This demarcation is also presented in the reference experimental data, where it is not based on strict thresholding or edge detection, but drawn from observing the soot cloud in motion [5] and is intended to aid the reader. For the simulation,

the envelopes are drawn separately for main- and post-injection soot and are obtained as iso-lines of a certain cut-off percentage of the local soot maxima, as discussed below.
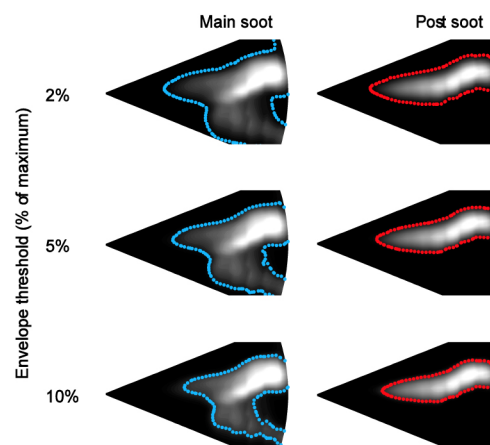

Figure 5. Three different thresholds for the "soot envelope", an iso-line of a certain cut-off percentage of the local soot maximum. Illustrated here is the planar soot volume fraction of the 18% O_2 case, at 14° CA. The blue dotted line indicates main injection while red indicates post-injection soot.

To distinguish between the soot from the main injection and the post-injection, a weighting of the total soot on *MF1/MFT* and *MF2/MFT* is performed (where *MFT=MF1+MF2*), consistently with the contribution of each mixture fraction to the total

equivalence ratio. Figure 5 shows the sensitivity of thus obtained envelopes (on both main- and post-injection soot) to the cut-off percentage employed. Three different thresholds for the soot envelope were tested for the figures to follow. In the previous figure, the corresponding envelopes are shown on the simulation reference case for only one representative time instant for brevity, at 374° CA. Note that the contour colour scales in Figure 5 are adjusted to enhance the clarity of visible contours; the post-injection soot volume fraction is actually around four times as high as the existing main-injection soot, for the time instant considered.

In general, the 2% level represents the broadest profile, but often includes unimportant regions of very low soot, obscuring the overall profile. The 10% criterion on the other hand is rather tightly fitted to the visible soot contours but is found to skip regions of considerable soot presence, especially disconnected regions. As a compromise, the remainder of the figures in this section use the threshold of 5% of the local maximum, to construct the soot cloud envelope.

The soot cloud structures predicted by CFD are presented along with the experimental data from NL and PLII imaging at three different time instants in Figure 6 and Figure 7 respectively, for the single-injection reference case with 18% O_2. The times selected, following [5], are those at which the direct interaction of the post-jet and main soot would have been observed in the case with post-injection. O'Connor and Musculus [5] showed the consistency of the measured soot envelopes between NL and PLII, being comparable with a slightly narrower soot region reported with PLII. The simulation also shows the same trend between CFD Integrated FvS and CFD Planar FvS. Therefore, for the post-injection case, only images of the CFD Integrated FvS will be considered, for comparison with experiment.
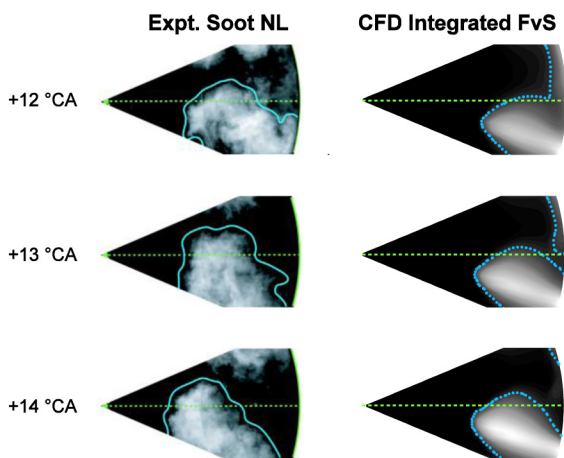

Figure 6. Single injection reference case: comparison of experimental soot-NL images with the line-of-sight integrated soot volume fraction from simulation The solid blue line represents an envelope of soot and is drawn by observing temporal data [5], while the dotted blue line represents an envelope based on 5% of the local maximum value.
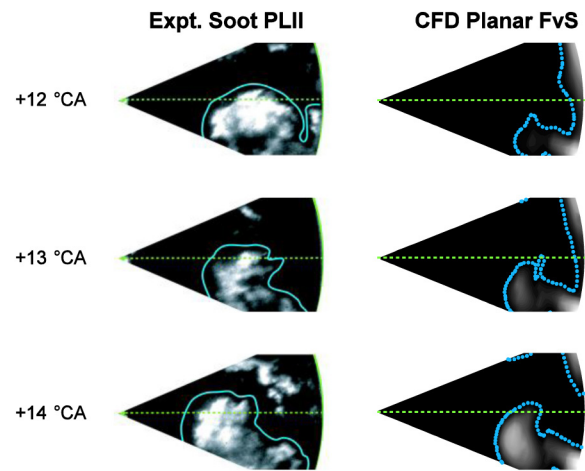

Figure 7. Single injection reference case: comparison of experimental soot-PLII images with the planar contours of soot volume fraction from simulation.

In Figure 6 and Figure 7 the orientation of the soot cloud results from impingement on the wall (before the times shown) and subsequent curling, a trend that is qualitatively well captured by CFD, except for the under-prediction of the return length travelled upstream (leftwards in the figures). The decrease in the area of contact with the wall as reflected in the NL-images is also reproduced, which is likely due to the oxidation of soot in the weak-soot areas (upper half of the figures, in the wall vicinity).

For the post-injection case similar comparisons can be made as illustrated in Figure 8. Some caution is to be recommended however, with respect to the comparison of actual soot cloud *extents*, bearing in mind that it is being carried out between instantaneous experimental images and Reynolds-averaged results from CFD.

It should be noted that the post-injection soot is fully contained within the post-injection soot "boundary" but this boundary does not contain post-injection soot exclusively; the head of this region contains soot (of lesser intensity) from the main injection that has most likely formed due to the mixture enrichment induced by the post-jet. The interaction of the main soot cloud with the post-injection jet increases the local total equivalence ratio, leading to an increase of soot associated simultaneously with both the main- and the post-injection as also observed in [29].

As is evident from the spatial distribution of the post-jet soot cloud (red contours), the simulation shows excellent prediction of the position of the post-injection soot with respect to penetration and orientation. At 12°CA the soot region of the main injection (blue contours) is qualitatively in agreement with both NL and PLII measurements. However, the computed post soot cloud is tighter and the minimal distance from the injector is considerably higher, in particular at 15 and 16°CA. Note that these time instants are after the end of post-injection, i.e. the dynamics of the injector closing play an important role [1].
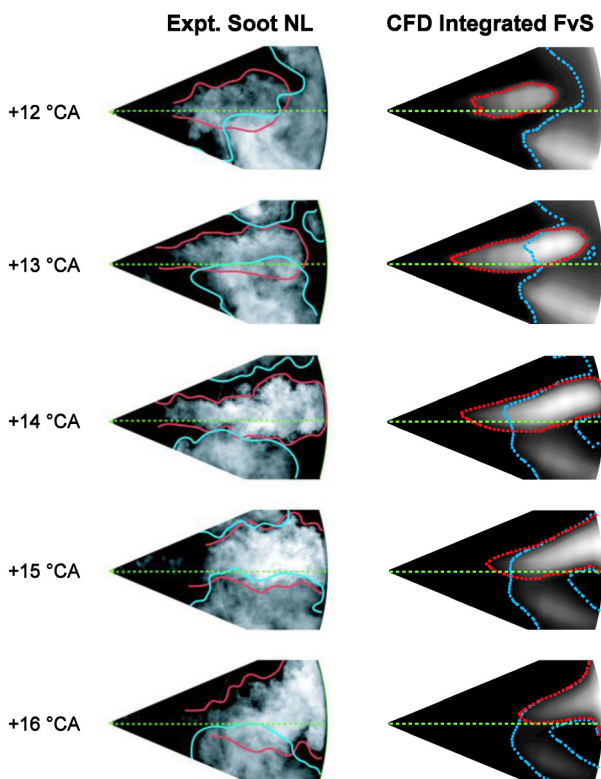
Figure 8. Post-injection reference case: comparison of experimental soot-NL images with the line-of-sight integrated soot volume fraction from simulation The solid blue and red lines represent an envelope of soot (from main- and post-injection respectively) and are drawn by observing temporal data [5], while the dotted blue and red lines represent an envelope of the same from simulation, based on a 5% threshold of the local maximum.

Effect of EGR on Post-Injection Effectiveness

This section presents a discussion on the influence of EGR on soot, with the goal of understanding the effectiveness of post-injection in the reduction thereof. The processes associated with the introduction of a post-injection are investigated and the role of the post-injection in affecting the soot formation and oxidation rates is assessed. Increased soot oxidation by post-injections is one of the mechanisms that has been argued to be responsible for overall soot reduction [4], and as will be discussed later, we suggest this increase is brought about by improved mixing around and within soot clouds, due to interaction with the post-jet.

Figure 9 shows the evolution of total soot mass in the cylinder for the 18% O_2 case. After reaching the peak, which occurs before the start of post-injection, the total soot from the post-injection case (solid line) initially rises compared to the single-injection (dashed line) due to additional soot formation from the post-injection, and as noted before, also due to the further enrichment of the main-injection fuel-rich gas by the post-jet, causing additional formation associated with both the main-and post-injection soot. Subsequently however, this effect is overwhelmed by accelerated oxidation rates, causing the soot mass in the post-injection case to fall to lower levels than the single injection case.
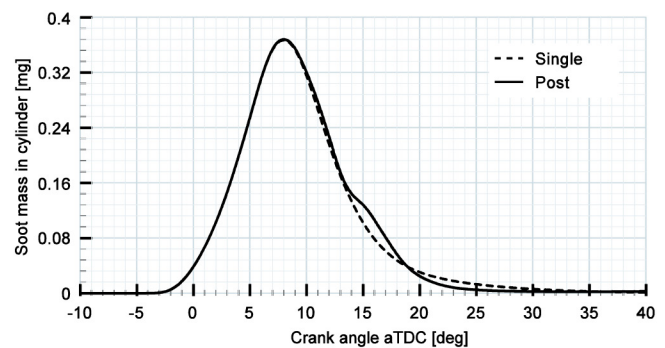

Figure 9. Evolution of total soot mass in cylinder for the reference case with 18% O_2.

To investigate further, we start by observing the total mixture fraction, temperature and soot volume fraction just after the start of the post-injection, for the four different EGR levels studied, shown in Figure 10. At the point just after the start of the post-injection (at 9° CA), the "tail" of the mixture fraction from the main-injection extends to the near vicinity of the incoming post-jet because of the close coupling. With increasing EGR however, this mixture fraction tail (illustrated by the blue dotted line in Figure 10) moves farther from the post-jet vicinity (black dotted line), despite the rich region of the first mixture fraction advancing towards it due to lower stoichiometry. The intermediate region, between the post-jet head and the main-mixture tail, is increasingly leaner as evidenced by the mixture fraction contours which are in the same scale across EGR levels.

Another observation concerns the temperature fields: the tail of the temperature profile advances towards the post-injection with increasing EGR, owing to the broader flame (red dotted line in Figure 10). At the high EGR levels, the tail of the main-injection flame extends very close to the post-jet, possibly causing early contact and premature ignition compared to the experiment, as reflected in the heat-release rate in Figure 4.

Variation in the computed soot volume fraction along the EGR sweep is modest (a factor of 3) and the higher maximum values are observed at intermediate oxygen concentrations. Similar observations were also made in [27] reporting cycle-resolved in-cylinder soot mass evolutions for different EGR levels. Note that quantitative soot mass measurements for the test cases in this study are not available. As expected, soot spatial extents correspond to the stoichiometry of the total mixture fraction, and given that the injected fuel mass does not change, the soot envelope is larger for higher-dilution cases.

In the following, the difference in oxygen distribution with and without post-injection is considered as shown in Figure 11 for two EGR levels: 18 and 12.6% O_2. Since we are interested in the relative enhancement of oxygen entrainment, this difference has been normalised by the distribution of the single-injection case at the same time instant. Inside the stoichiometric region of the post-injection, this quantity is expected to drop to the lower limit of −100%, which implies that the oxygen otherwise existing in the single-injection case has

been fully consumed by the introduction of the post-injection (for its own combustion). High positive values, on the other hand, imply that oxygen is transported inwards from other regions leading to accumulation. Such an accumulation is found at the tip of the post-injection as is evident from the transient evolution of this quantity illustrated in Figure 11.

For both EGR levels shown, no significant change in the oxygen concentration is seen outside the post-injection itself, for the first three time instants (9, 10, 11 °CA). As the spatial separation between the main- and the post-injection flames decreases, squeezing the intermediate region, a blob of additional oxygen is seen pushing itself across the edge of the

main flame region using the momentum of the post-jet. This blob propagates further downstream (as is clearly visible at 14° CA in Figure 11) to the regions close to the wall, where the main-injection soot is likely to be located (see Figure 10).

The relative entrainment effect can be orders of magnitude higher for the high-EGR cases as is evidenced by the strong blobs at 13° and 14° for the 12.6% O_2 case. This is attributed to the larger soot volume, extending closer to the injector and therefore allowing the post-injection to reach this position earlier and with higher momentum compared to the 18% O_2 reference case.
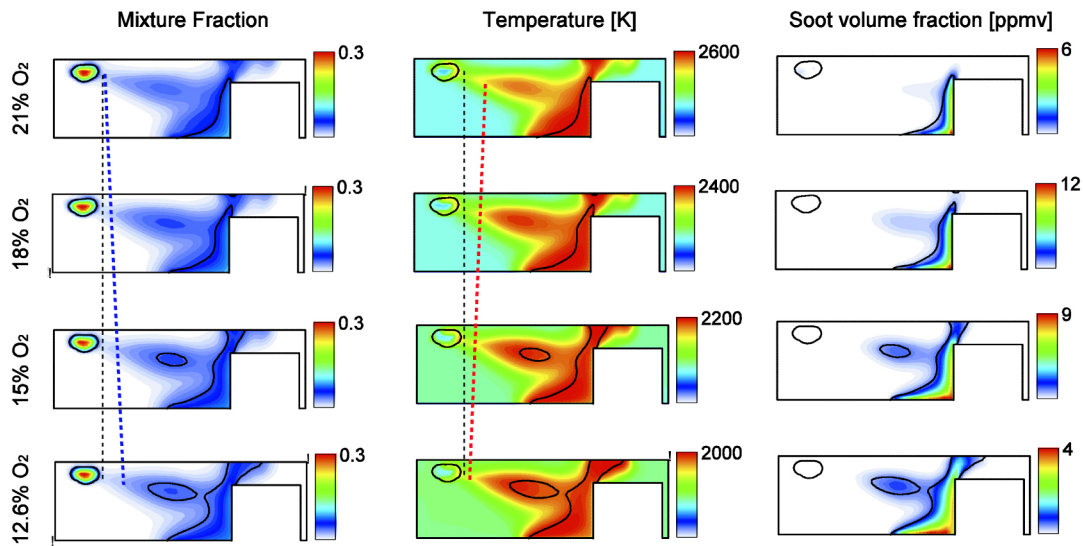

Figure 10. Total mixture fraction, temperature and soot volume fraction, shown just after the start of the post-injection (9° CA), over the four EGR levels studied. The solid black line represents the stoichiometric mixture fraction which is a function of the EGR level. The minimum for all colour scales is zero.
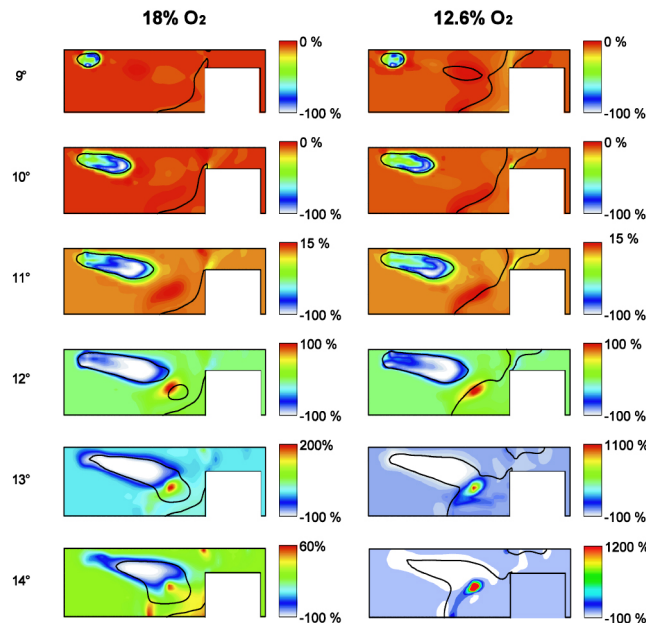

Figure 11. Relative difference in oxygen mass fraction between single-and post-injection cases (as a percentage of the oxygen mass fraction in the single-injection case). Positive regions indicate more oxygen transported inwards; negative regions imply oxygen is consumed for the post-injection's own combustion.

www.manaraa.com

One of the mechanisms enhancing the entrainment of oxygen is convection due to the increased momentum brought by the post-jet. Figure 12 shows the velocity differences between the single- and post-injection cases for the 18% O_2 reference case. It is evident (disregarding the increase *within* the post-jet) that the negative components around the tip of the post-jet are enhanced. This indicates enhanced flow of air from bowl-edge zones or squish zones towards the bowl where a major amount of soot is located. Small recirculation zones can also be identified, distinguished by localised increase or decrease of velocity in small spots, and this can also enhance convection. Supply of oxygen to the soot zones can be enhanced by even a slight increase in the velocity, and indeed the maximum change is only around 5 m/s. Small quantities of extra oxygen can have a major effect on the oxidation of soot due to the otherwise poor availability in the soot region, more strongly so at higher EGR as is well evident also in Figure 11.
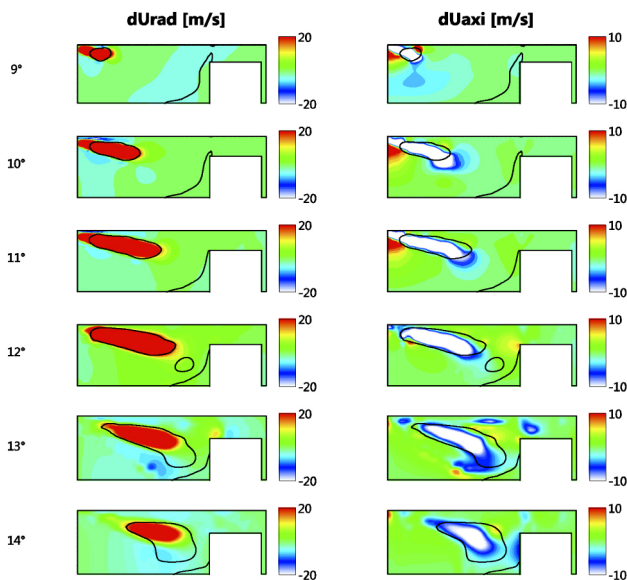

Figure 12. Radial (left) and axial (right) velocity differences between single- and post-injection cases for 18% O_2.

Contours of important soot-relevant quantities are examined in Figure 13 for the cases with 18% (upper) and 12.6% O_2 (lower). Quantities from top to bottom are: total mixture fraction, temperature, soot volume fraction, total soot formation rate, total soot oxidation rate and distinct soot oxidation rate by oxygen and OH. Distributions are drawn at 13° CA, when contact between post- and main-injection regions takes place. To enable a quantitative comparison, the quantities are plotted with their respective local minima and maxima. For the 18% O_2 case, the oxidation rate almost doubles following a large increase in the contribution of oxidation caused by O_2. While the soot formation rate maximum in the post-injection case increases roughly to four times that of the single injection (due to the added fuel), the oxidation rate due to O_2 increases to five times. However the OH-oxidation rate is unchanged, limiting the overall oxidation rate increase to a factor of two, since the OH-contribution is much more significant at this low EGR. For these reasons, the soot volume fraction is slightly increased,

but this increased soot appears within the post-injection, and it is anticipated that the oxidation rate should increase in the next time step due to oxygen entrainment (see 14° CA in Figure 11) providing for the oxidation of excess soot formed.

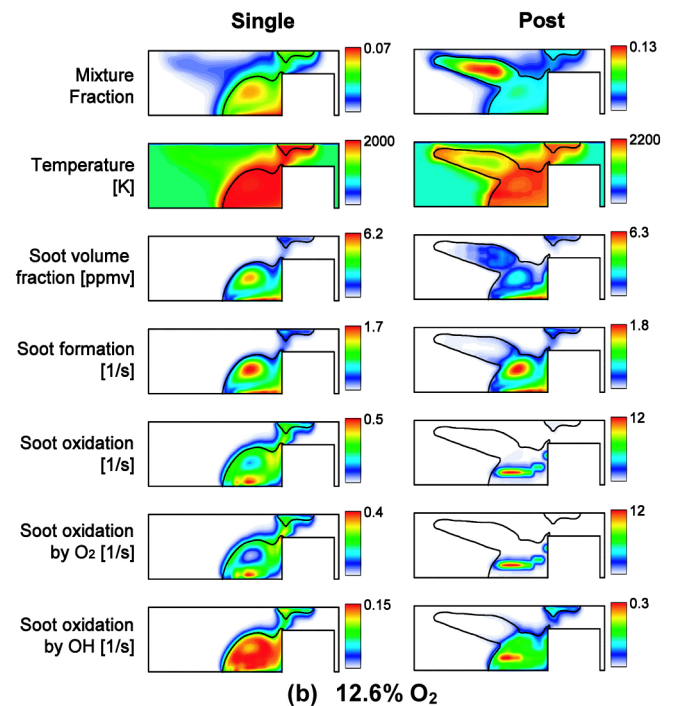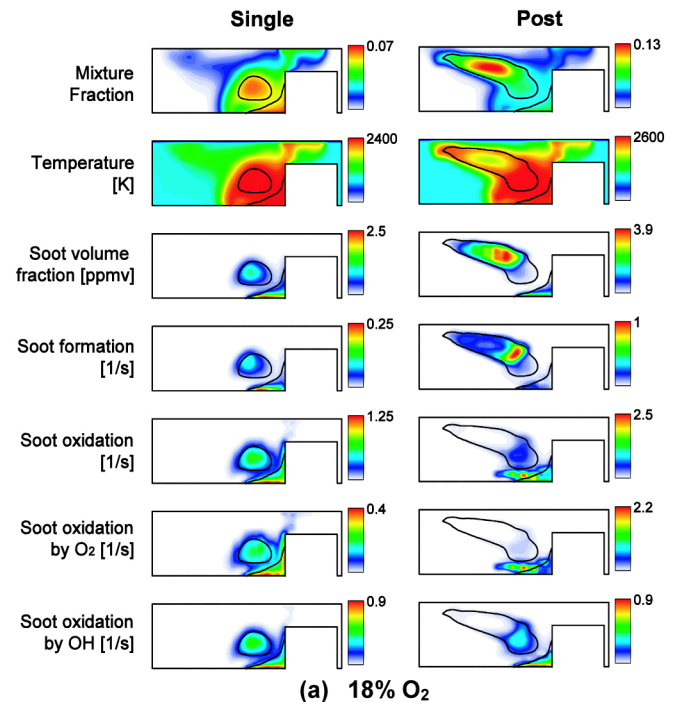(a) 18% O_2

(b) 12.6% O_2

Figure 13. Contours of selected fields at 13° CA (corresponding to the time instant of interaction between the post and main injection) on a vertical slice through the injector axis for the case with 18% oxygen (upper) and 12.6% oxygen (lower). (Left) single injection only, (Right) with post-injection.

More importantly, the increased O_2 driven oxidation shows a localised character, appearing slightly downstream of the maximum relative oxygen enhancement location. These observations are similarly investigated at the high-EGR level in the lower half of the same figure. Here, the soot oxidation rate due to O_2 increases by over an order of magnitude due to the post-injection. OH-oxidation offers a much smaller contribution to the total oxidation, relative to the reference case discussed previously. The OH-oxidation rate is also locally enhanced in a small region, but overall the oxidation rate increases mainly due to O_2 contribution and reaches the same order of enhancement. As before, the spots of soot oxidation by O_2 are highly localised. At this EGR level, the soot formation rate is strongly suppressed so that any increase from the post-injection is marginal, and the change in the overall soot volume fraction is minor. This strong inhibition of the formation rate is in agreement with the findings of [24] at a similar level of ambient O_2. It is observed that at low O_2 levels (high-EGR case), the O_2-oxidation plays a higher role in the overall oxidation, whereas OH-oxidation is predominant at high O_2-levels (reference case) due to the high temperature and correspondingly high OH levels, consistent with the findings of [23]. Low local temperatures due to EGR can lower the peak OH to one-fifth of that without EGR [27].

CONCLUSIONS

In this study, the influence of exhaust gas recirculation in a heavy-duty diesel engine on the interaction between post- and main- injection has been investigated numerically for four different levels of ambient dilution (12.6, 15, 18 and 21% O_2). Numerical simulations have been performed with the conditional moment closure (CMC) combustion model. An extended CMC formulation capable of accounting for multiple injections has been successfully employed. Computed apparent heat release rates were in very good agreement with the experiment except for the 12.6% O_2 case, where the predicted ignition of the post-injection was slightly too early. For the 18% O_2 reference case a direct comparison of the computed and measured temporal evolution of soot luminosity showed the spatial extents of the predicted post-injection soot cloud to be in good qualitative agreement with experimental data.

Subsequently, the model has been used to investigate the effect of the post-injection on in-cylinder soot evolution, especially with respect to the role of increased mixing; a detailed analysis highlighting the relative importance of soot formation and oxidation (both O_2 and OH contributions) is presented at two representative EGR levels. The local oxidation and formation rates for the post-injection case were found to show 'spotty' regions of surge due to mixing of the post jet with the pre-existing soot from the main injection. The surge in oxidation rate, which is caused by additional momentum imparted by the jet to the immediate vicinity, and the consequent entrainment of oxygen, can overwhelm the additional formation rate which results from the small further enrichment (at the head of the post-jet) of the already fuel-rich regions present from the main injection. This results in faster

oxidation, specifically O_2-oxidation, compared to the baseline single-injection case, especially at high EGR. At the time of main- and post-jet interaction, it can be seen that the contribution of O_2-oxidation towards the total oxidation rate remarkably increases with the addition of the post-injection, and that it occurs in spots of high intensity. Overall, the proposed extended CMC model along with integrated soot modelling appears to be a very promising framework for the study of close-coupled post-injection soot dynamics.

REFERENCES

1. Musculus, M.P.B., Miles P.C., and Pickett L.M., *Conceptual models for partially premixed low-temperature diesel combustion*. Progress in Energy and Combustion Science, 2013. 39(2-3): p. 246-283.

2. Idicheria, C. and Pickett, L., "Soot Formation in Diesel Combustion under High-EGR Conditions," SAE Technical Paper 2005-01-3834, 2005, doi:10.4271/2005-01-3834.

3. Tree, D.R. and Svensson K.I., *Soot processes in compression ignition engines*. Progress in Energy and Combustion Science, 2007. 33(3): p. 272-309.

4. O'Connor, J. and Musculus, M., "Post Injections for Soot Reduction in Diesel Engines: A Review of Current Understanding," *SAE Int. J. Engines* 6(1):400-421, 2013, doi:10.4271/2013-01-0917.

5. O'Connor, J. and Musculus M., *Effects of exhaust gas recirculation and load on soot in a heavy-duty optical diesel engine with close-coupled post injections for high-efficiency combustion phasing*. International Journal of Engine Research, 2014. 15(421).

6. Hessel, R., Reitz, R., Musculus, M., O'Connor, J. et al., "A CFD Study of Post Injection Influences on Soot Formation and Oxidation under Diesel-Like Operating Conditions," *SAE Int. J. Engines* 7(2):694-713, 2014, doi:10.4271/2014-01-1256.

7. Tap, F.A., et al., *A generalized flame surface density modelling approach for the auto-ignition of a turbulent non-premixed system*. Combustion Theory and Modelling, 2004. 8(1): p. 165-193.

8. Hasse, C. and Peters N., *A two mixture fraction flamelet model applied to split injections in a DI Diesel engine*. Proceedings of the Combustion Institute, 2005. 30: p. 2755-2762.

9. Haworth, D.C., *Progress in probability density function methods for turbulent reacting flows*. Progress in Energy and Combustion Science, 2010. 36(2): p. 168-259.

10. Barths, H., et al., *Simulation of combustion in direct injection diesel engines using a Eulerian particle flamelet model*. Proceedings of the Combustion Institute, 2000. 28: p. 1161-1168.

11. Molina, S., Desantes, J., Garcia, A., and Pastor, J., "A Numerical Investigation on Combustion Characteristics with the use of Post Injection in DI Diesel Engines," SAE Technical Paper 2010-01-1260, 2010, doi:10.4271/2010-01-1260.

12. Felsch, C., et al., *An extended flamelet model for multiple injections in DI Diesel engines*. Proceedings of the Combustion Institute, 2009. 32: p. 2775-2783.

13. Doran, E., Pitsch, H., and Cook, D., "Multi-Dimensional Flamelet Modeling of Multiple Injection Diesel Engines," SAE Technical Paper 2012-01-0133, 2012, doi:10.4271/2012-01-0133.

14. Doran, E.M., Pitsch H., and Cook D.J., *A priori testing of a two-dimensional unsteady flamelet model for three-feed combustion systems*. Proceedings of the Combustion Institute, 2013. 34: p. 1317-1324.

15. Kronenburg, A., *Double conditioning of reactive scalar transport equations in turbulent nonpremixed flames*. Physics of Fluids, 2004. 16(7): p. 2640-2648.

16. Kim, W.T. and Huh K.Y., *Numerical Simulation of Spray Autoignition By the First-order Conditional Moment Closure Model*. Proceedings of the Combustion Institute, 2002. 29: p. 569-576.

17. Wright, Y.M., et al., *Simulations of spray autoignition and flame establishment with two-dimensional CMC*. Combustion and Flame, 2005. 143(4): p. 402-419.

18. Wright, Y.M., et al., *Experiments and Simulations of n-Heptane Spray Auto-Ignition in a Closed Combustion Chamber at Diesel Engine Conditions*. Flow Turbulence and Combustion, 2010. 84(1): p. 49-78.

19. Bolla, M., Gudmundsson, T., Wright, Y., and Boulouchos, K., "Simulations of Diesel Sprays Using the Conditional Moment Closure Model," *SAE Int. J. Engines* 6(2):1249-1261, 2013, doi:10.4271/2013-01-1618.

20. Borghesi, G., et al., *Modeling evaporation effects in conditional moment closure for spray autoignition*. Combustion Theory and Modelling, 2011. 15(5): p. 725-752.

21. Wright, Y., Boulouchos, K., De Paola, G., and Mastorakos, E., "Multi-dimensional Conditional Moment Closure Modelling Applied to a Heavy-duty Common-rail Diesel Engine," *SAE Int. J. Engines* 2(1):714-726, 2009, doi:10.4271/2009-01-0717.

22. De Paola, G., et al., *Diesel engine simulations with multi-dimensional conditional moment closure*. Combustion Science and Technology, 2008. 180(5): p. 883-899.

23. Bolla, M., et al., *Soot Formation Modeling of n-Heptane Sprays Under Diesel Engine Conditions Using the Conditional Moment Closure Approach*. Combustion Science and Technology, 2013. 185(5): p. 766-793.

24. Farrace, D., Bolla, M., Wright, Y., and Boulouchos, K., "Predicting In-Cylinder Soot in a Heavy-Duty Diesel Engine for Variations in SOI and TDC Temperature Using the Conditional Moment Closure Model," *SAE Int. J. Engines* 6(3):1580-1593, 2013, doi:10.4271/2013-24-0016.

25. Bolla, M., et al., *Modeling of soot formation in a heavy-duty diesel engine with conditional moment closure*. Fuel, 2014. 117: p. 309-325.

26. Bolla, M., Wright Y.M., and Boulouchos K.. *Application of a Conditional Moment Closure Combustion model to a large two-stroke marine Diesel engine reference experiment*. in *the 8th International Conference on Modeling and Diagnostics for Advanced Engine Systems (COMODIA)*. 2012. Fukuoka, Japan.

27. Farrace, D., Bolla, M., Wright, Y., and Boulouchos, K., "Numerical Study of the Influence of EGR on In-Cylinder Soot Characteristics in a Heavy-Duty Diesel Engine using CMC," *SAE Int. J. Engines* 7(1):256-268, 2014, doi:10.4271/2014-01-1134.

28. Bolla, M., et al., *An Extended CMC Model for Multiple Injections in Diesel Engines*. Combustion Theory and Modelling (submitted), 2014.

29. Frapolli, N., Bolla, M., Boulouchos, K., and Wright, Y., "Simulations of In-cylinder Processes in a Diesel Engine Operated with Multiple-injections Using an Extended CMC Model," SAE Technical Paper 2014-01-2571, 2014, doi:10.4271/2014-01-2571.

30. Bolla, M., et al., *An Extended CMC Model for the Simulation of Diesel Engines with Multiple Injections*, in *International Multidimensional Engine Modeling Users' Group Meeting*. 2014: Detroit, Michigan.

31. CD-adapco. *STAR-CD*. 2014 [cited 2014 Jan 14]; Available from: http://www.cd-adapco.com/products/.

32. Reitz, R. and Diwakar, R., "Effect of Drop Breakup on Fuel Sprays," SAE Technical Paper 860469, 1986, doi:10.4271/860469.

33. Bilger, R.W., *Conditional Moment Closure for Turbulent Reacting Flow*. Physics of Fluids a-Fluid Dynamics, 1993. 5(2): p. 436-444.

34. Klimenko, A.Y. and Bilger R.W., *Conditional Moment Closure for Turbulent Combustion*. Progress in Energy and Combustion Science, 1999. 25(6): p. 595-687.

35. O'Brien, E.E. and Jiang T.L., *The Conditional Dissipation Rate of an Initially Binary Scalar in Homogeneous Turbulence*. Physics of Fluids a-Fluid Dynamics, 1991. 3(12): p. 3121-3123.

36. Liu, S., et al., *Effects of Strain Rate on High-Pressure Nonpremixed n-Heptane Autoignition in Counterflow*. Combustion and Flame, 2004. 137: p. 320-339.

37. Leung, K.M., Lindstedt R.P., and Jones W.P., *A Simplified Reaction-Mechanism for Soot Formation in Nonpremixed Flames*. Combustion and Flame, 1991. 87(3-4): p. 289-305.

CONTACT INFORMATION

Sushant S. Pandurangi
ETH Zürich, ML L 18
Sonneggstrasse 3
8092 Zürich, Switzerland
sushpa@lav.mavt.ethz.ch
http://www.lav.ethz.ch

ACKNOWLEDGEMENTS